communications materials

ARTICLE

https://doi.org/10.1038/s43246-022-00290-y OPEN

Hybrid molecular beam epitaxy of germanium-based oxides

Fengdeng Liu[1,6], Tristan K. Truttmann[1,6], Dooyong Lee[1], Bethany E. Matthews[2], Iflah Laraib[3], Anderson Janotti[3], Steven R. Spurgeon[2,4], Scott A. Chambers[5] & Bharat Jalan[1]✉

Germanium-based oxides such as rutile GeO_2 are garnering attention owing to their wide band gaps and the prospects of ambipolar doping for application in high-power devices. Here, we present the use of germanium tetraisopropoxide (GTIP), a metal-organic chemical precursor, as a source of germanium for the demonstration of hybrid molecular beam epitaxy for germanium-containing compounds. We use $Sn_{1-x}Ge_xO_2$ and $SrSn_{1-x}Ge_xO_3$ as model systems to demonstrate our synthesis method. A combination of high-resolution X-ray diffraction, scanning transmission electron microscopy, and X-ray photoelectron spectroscopy confirms the successful growth of epitaxial rutile $Sn_{1-x}Ge_xO_2$ on TiO_2(001) substrates up to $x = 0.54$ and coherent perovskite $SrSn_{1-x}Ge_xO_3$ on $GdScO_3$(110) substrates up to $x = 0.16$. Characterization and first-principles calculations corroborate that germanium occupies the tin site, as opposed to the strontium site. These findings confirm the viability of the GTIP precursor for the growth of germanium-containing oxides by hybrid molecular beam epitaxy, thus providing a promising route to high-quality perovskite germanate films.

[1] Department of Chemical Engineering and Materials Science, University of Minnesota, Minneapolis, MN 55455, USA. [2] Energy and Environment Directorate, Pacific Northwest National Laboratory, Richland, WA 99352, USA. [3] Department of Materials Science and Engineering, University of Delaware, Newark, DE 19716, USA. [4] Department of Physics, University of Washington, Seattle, WA 98195, USA. [5] Physical and Computational Sciences Directorate, Pacific Northwest National Laboratory, Richland, WA 99352, USA. [6] These authors contributed equally: Fengdeng Liu, Tristan K. Truttmann. ✉email: bjalan@umn.edu

The holy grail of semiconductor heterostructures is the ability to produce high-quality semiconductor films with tunable bandgaps that are also lattice-matched to commercially available substrates. One common strategy to achieve this is to alloy two or more semiconductors and judiciously choose the alloy composition for the desired bandgap and lattice parameter. In principle, this approach can be applied to the alkaline-earth stannates, a system of three materials (namely $CaSnO_3$, $SrSnO_3$, and $BaSnO_3$) that has recently fascinated researchers for potential applications in next-generation power electronics and ultraviolet optoelectronics. The alloys of these three materials, whose crystal structures are summarized in Fig. 1b, span the purple shaded region of bandgaps (E_g) and pseudocubic lattice parameters (a) in Fig. 1a. However, the scarcity of commercially available substrates makes the range of accessible bandgaps in lattice-matched systems rather limited. The use of $GdScO_3$ as the substrate facilitates the largest bandgap range for lattice-matched alloys. However, the span is only 0.1 eV, from $E_g = 4.2$ eV ($Ba_{0.13}Ca_{0.87}SnO_3$) to $E_g = 4.3$ eV ($Sr_{0.26}Ca_{0.74}SnO_3$). Such a limited bandgap range provides few opportunities for modulation doping using lattice-matched oxide heterostructures.

Adding a second tuning parameter to this material system would expand the gamut of accessible properties. Replacement of Sn with Ge offers one such tuning parameter. Oxides containing Ge^{4+} typically have conduction bands derived from Ge 4*s* orbitals, which, analogous to Sn 5*s* orbitals, produce dispersive conduction bands with low electron-effective masses. However, the different sizes and energies of the atomic orbitals lead to nuanced differences in the physical and electronic structures. This variation has been exploited in rutile oxides, where the substitution of Sn with Ge yields semiconductors with bandgaps ranging from 3.6 to 4.7 eV[1] with predicted ambipolar doping, offering encouraging prospects as ultrawide bandgap (UWBG) semiconductors for power electronics[2–7].

The crystal structures of alkaline-earth germanates are summarized in Fig. 1c. While perovskite $BaGeO_3$—a chemical analog to $BaSnO_3$—has not yet been synthesized, it is predicted to be metastable in the cubic structure[8]. The cubic perovskite $SrGeO_3$ has been successfully synthesized by a high-pressure, high-temperature method and quenched to ambient conditions; it displays an indirect bandgap $E_g = 2.7$ eV, but its wider direct bandgap (3.5 eV) makes it transparent to visible light[9]. $SrGeO_3$ has also been doped with La, yielding room-temperature mobility of 12 $cm^2 V^{-1} s^{-1}$ (see ref. [9]). However, DFT calculations suggest that both $SrGeO_3$ and $BaGeO_3$ have the potential to achieve phonon-limited mobilities superior to those of $BaSnO_3$[8]. Finally, $CaGeO_3$ has a metastable orthorhombic perovskite structure quenchable to ambient conditions. Although this material has not been optically or electrically characterized, it is almost certainly a transparent semiconductor with $E_g > 2.7$ eV[10–13].

The yellow region in Fig. 1a shows the additional range of E_g and a made available by adding $SrGeO_3$ to the stannate alloy system. We note that the region encompasses nearly all commercially available perovskite oxide substrates, and alloys lattice-matched to $DyScO_3$ substrates have bandgaps that span 1.5 eV, from $E_g = 2.9$ eV ($Ba_{0.49}Sr_{0.51}Sn_{0.49}Ge_{0.51}O_3$) to $E_g = 4.4$ eV ($Sr_{0.07}Ca_{0.93}SnO_3$), providing ample opportunity for lattice-matched heterostructures in modulation-doping field-effect transistors (MODFET) and, potentially, even optoelectronic devices.

Molecular beam epitaxy (MBE) is considered a gold-standard technique to grow high-quality heterostructures. However, since MBE relies on the codeposition or shuttered growth of individual elements, achieving a composition with a target E_g and a while simultaneously maintaining the A:B-site cation stoichiometry presents a formidable challenge in flux calibration. Therefore, it is desirable to use adsorption-controlled growth, which exploits thermodynamics to automatically regulate the A:B-site cation stoichiometry. Hybrid MBE is a technique that draws on the high vapor pressure of metal–organic precursors to achieve adsorption-controlled growth. It has been successfully applied to the adsorption-controlled growth of titanates[14], vanadates[15], and stannates[16]. However, it has not yet been applied to the growth of Ge-containing oxides. Although ozone-assisted MBE growth using germanium-suboxide as a source of germanium has recently been demonstrated[5], hybrid MBE may offer additional advantages: (1) there is no need to break growth chamber vacuum to replace materials; (2) oxygen-containing precursor provides an additional source of oxygen, and therefore, eliminates the need of ozone; (3) since the chemical precursor is not directly kept inside the UHV chamber, it eliminates the possibility of source oxidation (and hence the flux instability).

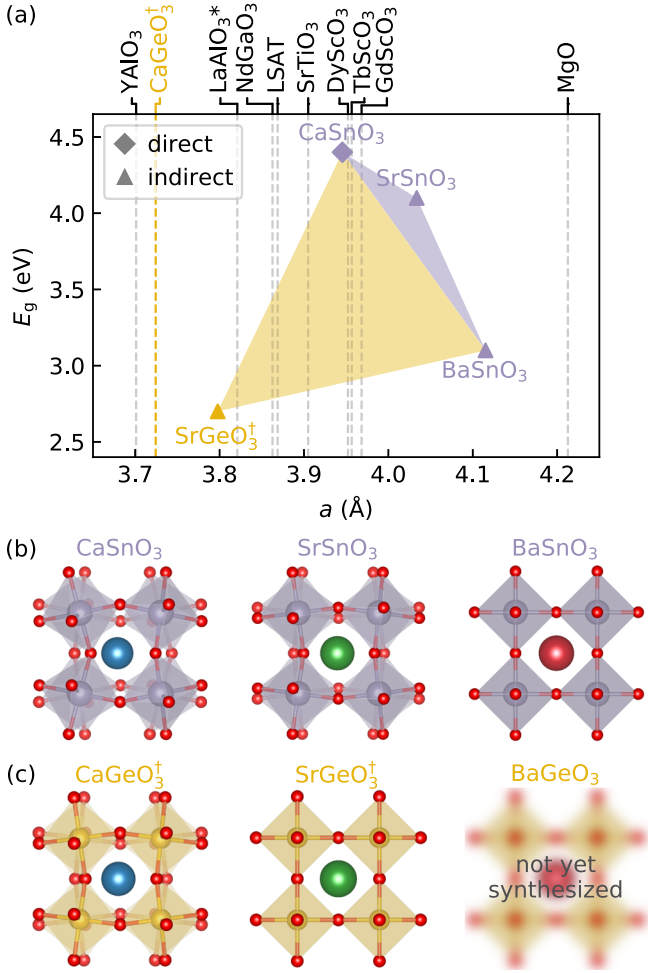

Fig. 1 Summary of alkaline-earth stannates and alkaline-earth germanates. a Bandgap (E_g) vs pseudocubic lattice parameter (a) of alkaline-earth stannates and alkaline-earth germanates, $SrGeO_3$. The purple shaded region represents values of E_g and a that are available to alloys of the three materials. The yellow region represents those additional values that are available when including perovskite $SrGeO_3$ in the alloy system. The lattice parameters of commercially available substrates are shown as vertical lines. **b** Crystal structures of alkaline-earth stannates. **c** Crystal structures of alkaline-earth germanates. All stannate perovskite structures are from ref. [37]. The $CaGeO_3$ structure is from ref. [10]. The $SrGeO_3$ structure is from ref. [26]. †Denotes metastable crystal structures that were quenched to ambient conditions. *Denotes a rhobohedral distortion at room temperature.

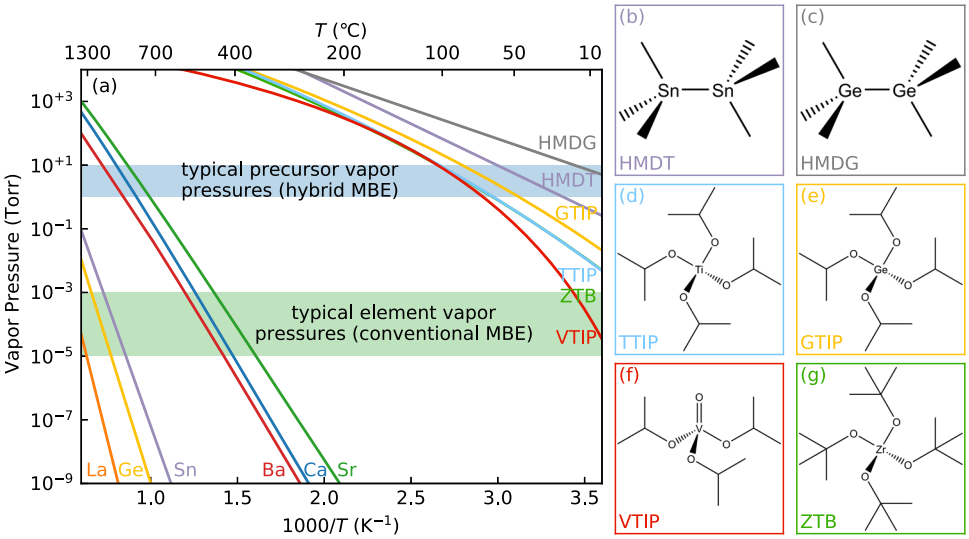

Fig. 2 Vapor pressures and structures of metal–organic precursors. a Vapor pressures of common elements in Ge-based oxides compared to precursors for hybrid MBE. **b**–**g** The chemical structures of the precursors including hexamethylditin (HMDT, **b**)[16,38], hexamethyldigermanium (HMDG, **c**), titanium tetraisopropoxide (TTIP, **d**)[39,40], germanium tetraisopropoxide (GTIP, **e**), vanadium oxytriisopropoxide (VTIP, **f**)[41], and zirconium *tert*-butoxide (ZTB, **g**)[42,43]. All metal vapor pressures use the equations from Alcock and coworkers[44]. Ge uses a fit to data from ref. 45. The vapor pressures for GTIP, TTIP, and VTIP use Antoine parameters from ref. [46] who themselves took this data from ref. [47]. HMDT data use the enthalpy of vaporization from ref. [48] and the standard entropy of vaporization fit to boiling temperatures from chemical suppliers. HMDG data use Trouton's rule along with a boiling temperature provided from Sigma-Aldrich.

Here, we report on a hybrid MBE approach for the growth of Ge-based oxides using germanium tetraisopropoxide (GTIP) as a metal–organic precursor for Ge. Figure 2 shows that GTIP has a much higher vapor pressure than elemental Ge. GTIP only requires temperatures as low as 50–100 °C whereas elemental Ge requires significantly higher temperatures (>1000 °C) to achieve sufficient flux. Furthermore, GTIP vapor pressure is also comparable to established hybrid MBE metal–organic precursors. We chose $Sn_{1-x}Ge_xO_2$ and $SrSn_{1-x}Ge_xO_3$ as model systems to demonstrate the use of GTIP in the growth of binary and ternary oxides, successfully synthesizing epitaxial rutile $Sn_{1-x}Ge_xO_2$ and coherent perovskite $SrSn_{1-x}Ge_xO_3$ films. Phase-pure rutile GeO_2 and perovskite $SrGeO_3$ were not chosen for this study as they may require epitaxial stabilization and therefore, will be a subject of future study.

Results and discussion

AFM and XRD results of Ge-based oxides. Figure 3a shows AFM of rutile $Sn_{1-x}Ge_xO_2/TiO_2(001)$ with different Ge concentrations. Increasing the germanium fraction x from 0 to 0.54 decreased the root mean square (RMS) roughness from 1373 to 461 pm. Supplementary Note 1 discusses the delicate interplay among film composition, film thickness, and surface roughness.

Figure 3b shows the rutile HRXRD 2θ-ω coupled scans and corresponding rocking curves around the (002) film peaks. The 2θ-ω coupled scans show that the film lattice parameters decrease with Ge incorporation, consistent with Ge's smaller ionic radius. The full width at half maximum (FWHM) of each film decreases from 0.93° to 0.086° as Ge incorporation increases from 0 to 0.54. This goes against the intuitive expectation that adding Ge would increase the structural disorder by disrupting translational symmetry through random substitution. It is also noteworthy that these rocking curves appear to be a linear combination of two Gaussians (a narrow and a broad component). In the discussion of the RSMs below, we explain both observations in terms of strain relaxation.

Figure 3c shows AFM images of $SrSn_{1-x}Ge_xO_3/GdScO_3(110)$ with different Ge concentrations. These micrographs show surface roughnesses that decrease with Ge incorporation from 503 to 171 pm. Unlike the rutile samples, however, this trend cannot be explained by film thickness. Instead, the perovskite film thickness is not affected by Ge incorporation, suggesting the Sn-species desorption is not affected by Ge incorporation in this material system. This is likely a result of the higher thermodynamic stability of the perovskite system compared to the rutile system. The decreased surface roughness with Ge incorporation might instead be explained by other factors, such as modified adatom mobility or a decreased driving force for adatom agglomeration.

Figure 3d shows the HRXRD 2θ-ω coupled scans and corresponding rocking curves around the perovskite $(002)_{pc}$ film peak. The 2θ-ω coupled scans demonstrate that the replacement of Sn with Ge decreases the film lattice parameters, consistent with smaller Ge^{4+} at the Sn^{4+} site. The Kiessig fringes and rocking curve FWHM of 0.07–0.08° demonstrate uniform films with high structural quality.

To investigate how Ge incorporation influences the strain relaxation of these films, we measured reciprocal space maps of both the rutile and perovskite samples. Figure 4a–c shows the RSMs around the (202) reflection of the rutile films. Contours and guidelines have been added to show the expected peak position depending on composition and strain, following a similar procedure used for (Al,Ga)N heterostructures by Enslin and coworkers[17]. Each contour represents all possible strains at a single composition, and the two guidelines represent all possible compositions for fully coherent and fully relaxed films. For the SnO_2 film in Fig. 4a, the film peak is centered over the $x = 0$ contour, close to where it intersects the relaxed guideline suggesting a nearly complete film relaxation.

For the film in Fig. 4b, the film peak resides slightly north of the $x = 0.25$ contour, consistent with the $x = 0.28$ Ge fraction determined from XPS. Furthermore, the peak lies between the relaxed and coherent guidelines, indicating the film is compressively strained and has undergone a small degree of relaxation toward its bulk lattice parameter. For the $x = 0.54$ film in Fig. 4c, the film peak resides directly over the coherent guideline,

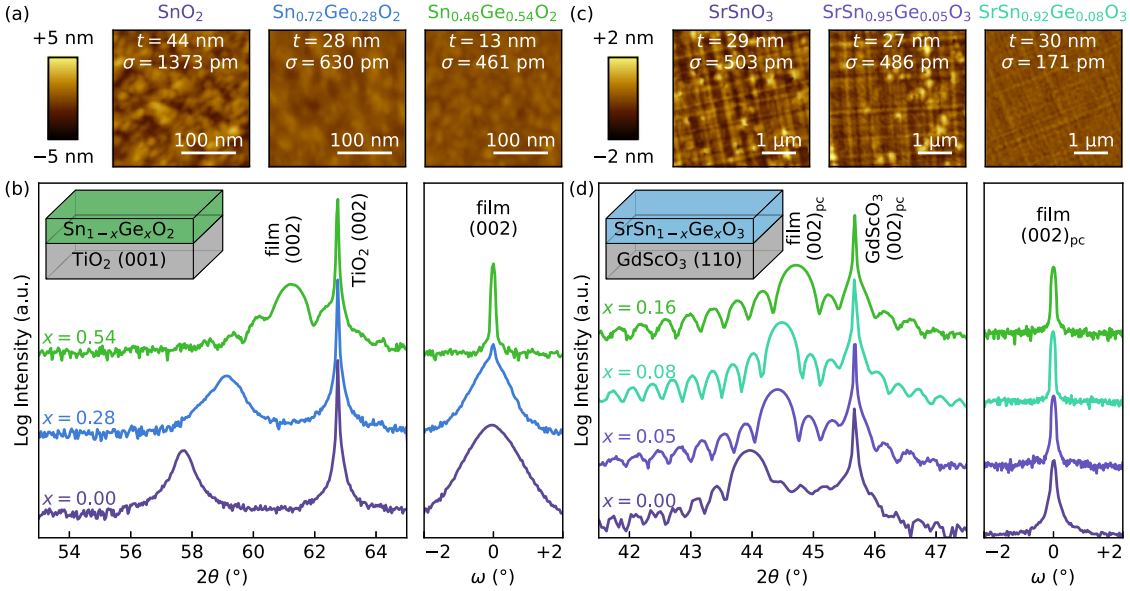

Fig. 3 Surface morphology and structural quality of Ge-based oxides. a Atomic force microscopy (AFM) of $Sn_{1-x}Ge_xO_2/TiO_2$ (001) films showing smooth film surfaces. **b** Room-temperature high-resolution X-ray diffraction (HRXRD) 2θ-ω coupled scans and rocking curves around the (002) film peak of $Ge_xSn_{1-x}O_2/TiO_2$(001) films. **c** AFM images of $SrGe_xSn_{1-x}O_3/GdScO_3$(110) showing film surfaces that get smoother with Ge incorporation. **d** Room-temperature HRXRD 2θ-ω coupled scans and rocking curves around the $(002)_{pc}$ film peak of $SrGe_xSn_{1-x}O_3/GdScO_3$(110). The insets of (**b**, **d**) show the film structures.

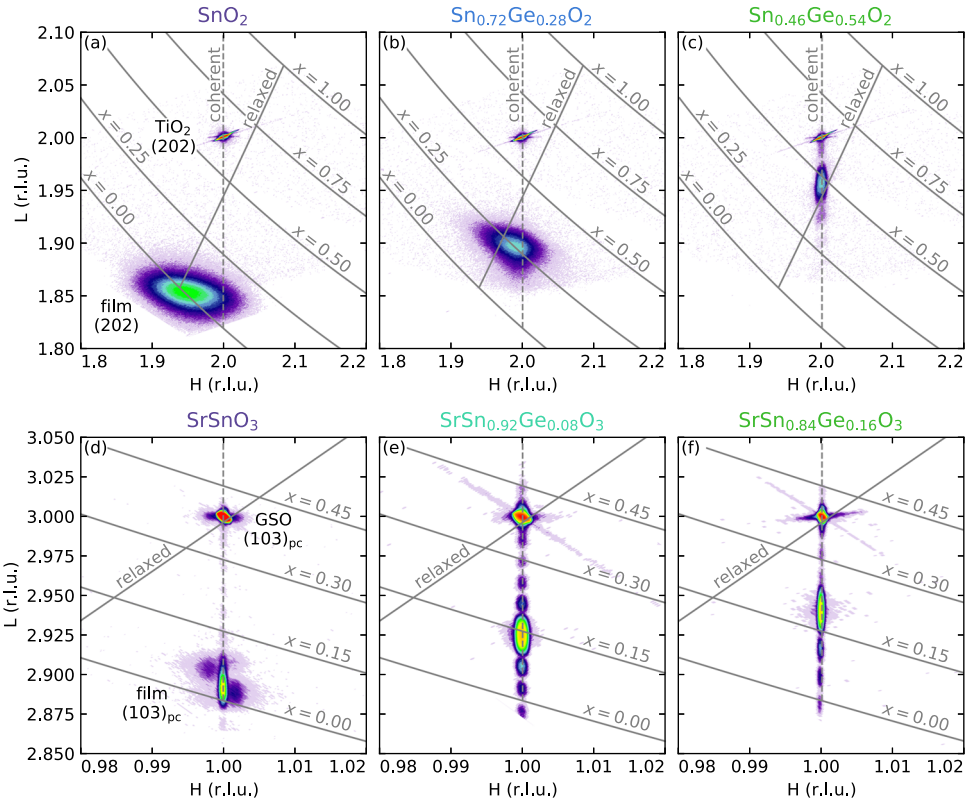

Fig. 4 Reciprocal space maps of Ge-based oxides. a–**c** Reciprocal space maps (RSMs) of rutile $Ge_xSn_{1-x}O_2/TiO_2$ (001) films in the (202) region. **d**–**f** RSMs of perovskite $SrGe_xSn_{1-x}O_3/GdScO_3$ (110) films in the $(103)_{pc}$ region. All RSMs include composition contours and relaxed/coherent guidelines to show the expected peak positions based on composition and strain.

indicating a film that is completely tensile strained to the substrate. The reader may notice that the film is expected to lie north of the $x = 0.50$ contour but is in fact south of it. This small discrepancy is mostly likely due to small deviations from Vegard's law, which was used to calculate the positions of these contours. This discrepancy may also be caused by an error in the composition determined from XPS.

The progression from a nearly fully relaxed film at $x = 0$ to a fully strained film at $x = 0.54$ can be explained by considering two facts. First, the growth rates decrease with Ge incorporation, so

higher values of x correspond to thinner films that have less built-up elastic strain energy. Second, films with higher Ge fractions have smaller lattice parameters, better matching the TiO_2 substrate, also resulting in less elastic strain energy. The resulting trend in strain relaxation fully explains why Ge incorporation improves the rocking curves in Fig. 3b. The two-Gaussian-shaped rocking curve is a well-understood phenomenon commonly observed during the strain relaxation of epitaxial films[18].

The RSMs of three representative perovskite films are shown in Fig. 4d–f. Unlike the rutile films, each perovskite film is fully strained to the $GdScO_3$ substrate. Again, one may notice small deviations between the film peak positions and their expected position based on the composition contours. For example, the $x = 0$ film peak in Fig. 4d is slightly north of the $x = 0$ contour. These discrepancies are probably due to a lack of accurate experimental Poisson ratios used to calculate the contours.

Valence state and occupation site of Ge in Ge-based oxides. One major challenge associated with the growth of high-quality oxides containing late transition metals (like Ru, Ni, and Cu) or main group metals (like Bi, Ge, and Sn) is achieving full oxidation of these high-electronegativity metals. To investigate the oxidation of Ge, we performed XPS on the rutile and perovskite films. Figure 5a shows Ge 3*d* core-level spectra of rutile films compared to that of a Ge reference wafer with native oxide; we mark the Ge 3*d* binding energy of different valence states for comparison, as shown at the top of Fig. 5a, b using assignments from Molle and coworkers[19]. We can clearly see that film peak position matches the Ge^{4+} position in the reference wafer, suggesting that Ge stays in the 4+ state in which it is delivered via GTIP.

In the XPS of the perovskite samples shown in Fig. 5b, however, the film peak position better matches the Ge^{3+} position in the reference wafer, which suggests that Ge is in the 3+ state. However, this is unlikely because Ge is generally not stable in the 3+ state. The Ge in the reference wafer was oxidized by exposure to air where oxidation is limited by solid-state diffusion. Hence, the reference wafer can achieve the otherwise unattainable oxidation states of 1+ and 3+, which still only constitute a very small fraction of the analyzed volume. We posit that the unusual coordination environment for Ge in the perovskite structure results in a different binding energy for B-site Ge^{4+} than is observed in amorphous GeO_2 due to differences in total electrostatic potential.

To determine the coordination environment of the Ge in the $SrSnO_3$ host lattice, cross-sectional STEM was performed. Figure 5c shows STEM-HAADF images of two perovskite samples, in which image intensity scales with atomic number ($Z^{\sim 1.7}$). The images show high-quality interfaces free of dislocations, consistent with the conclusion of fully coherent films determined from RSMs in Fig. 4e, f. The $x = 0.08$ sample shows a subtle low-Z band at the interface. This feature might be a result of slight A:B-site nonstoichiometry due to effusion cell or substrate temperature transients caused by opening the shutter at the beginning of growth. Figure 5d shows atomic-resolution STEM-EDS and STEM-EELS elemental maps and line profiles of Ge, Sr, and Sn. The line profiles show clear alignment of Ge and Sn peaks occurring in the valleys of the Sr signal, demonstrating direct substitution of Sn with Ge on the B-site. Therefore, our experimental data indicate that Ge resides in an octahedral coordination environment in the perovskite lattice.

To further examine the site preference of Ge, we have carried out DFT calculations to determine the formation enthalpy of Sr_{1-}

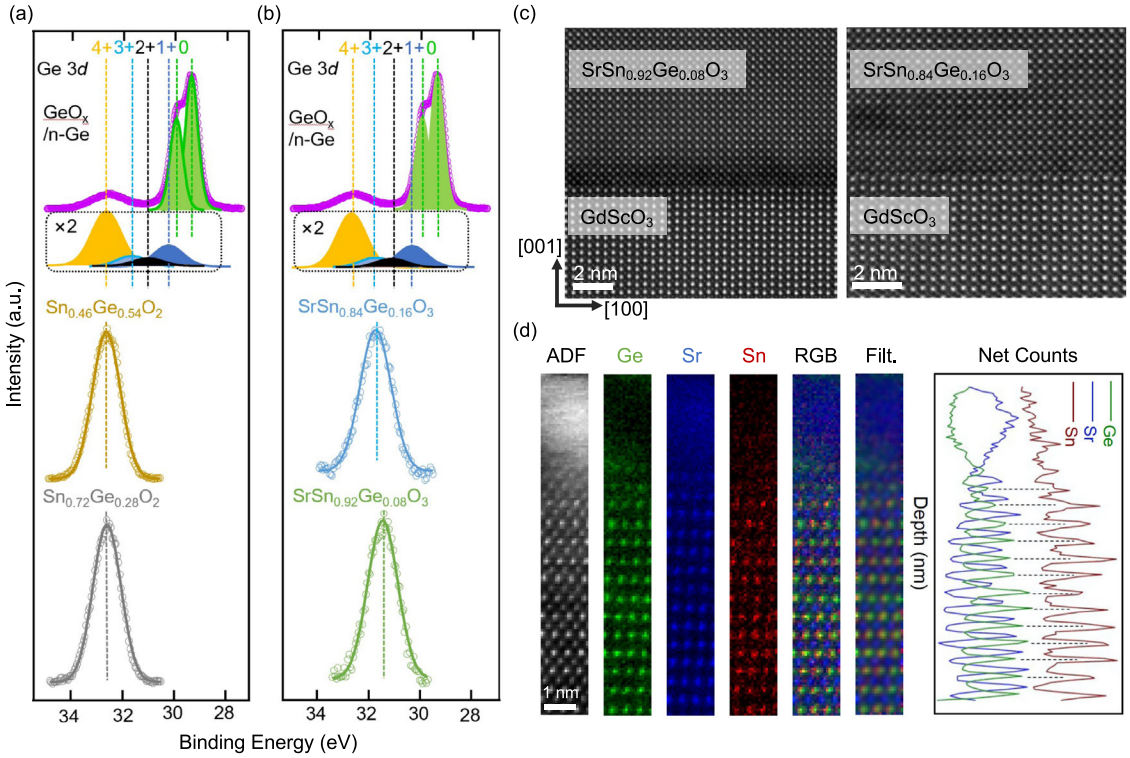

Fig. 5 Valence state and site occupation of Ge in Ge-based oxides. a, **b** Ge 3*d* core-level hard X-ray photoelectron spectra (HAXPES) of $Sn_{1-x}Ge_xO_2/TiO_2$ (001) films (**a**) and $SrGe_xSn_{1-x}O_3/GdScO_3$(110) films (**b**). The top of (**a**, **b**) shows a GeO_x/n-Ge reference wafer to assist in oxidation state determination. The suboxide spectrum was vertically offset and expanded ×2. **c** Drift-corrected high-angle annular dark-field scanning transmission electron micrographs (STEM-HAADF) of the $SrGe_xSn_{1-x}O_3/GdScO_3$ interfaces. **d** Energy dispersive X-ray spectroscopy (STEM-EDS) of the Sn *L* peak and electron energy-loss spectroscopy (STEM-EELS) of the Sr *L* and Ge *L* edges. Composite maps and integrated line profiles of the $SrSn_{0.84}Ge_{0.16}O_3$ film show clear alignment of Sn and Ge signals.

$_x$Ge$_x$SnO$_3$ (referred to as A-site alloys) and SrSn$_{1-x}$Ge$_x$O$_3$ (referred to as B-site alloys) as a function of Sn, Ge, and Sr chemical potentials. We can define the preference of Ge occupying Sr- vs. Sn site by taking the difference in the formation enthalpies of A-site and B-site alloys as a function of Sn and O chemical potentials, such as:

$$\Delta H^{\mathrm{f}}\left[\mathrm{Sr}_{1-x}\mathrm{Ge}_x\mathrm{SnO}_3\right] = E_{\mathrm{t}}\left[\mathrm{Sr}_{1-x}\mathrm{Ge}_x\mathrm{SnO}_3\right] - E_{\mathrm{t}}\left(\mathrm{SrSnO}_3\right) + \left[(1-x)E_{\mathrm{t}}(\mathrm{Sr}) + \mu_{\mathrm{Sr}}\right] - x\left[E_{\mathrm{t}}(\mathrm{Ge}) + \mu_{\mathrm{Ge}}\right] \quad (1)$$

and

$$\Delta H^{\mathrm{f}}\left[\mathrm{SrSn}_{1-x}\mathrm{Ge}_x\mathrm{O}_3\right] = E_{\mathrm{t}}\left[\mathrm{SrSn}_{1-x}\mathrm{Ge}_x\mathrm{O}_3\right] - E_{\mathrm{t}}\left(\mathrm{SrSnO}_3\right) + \left[(1-x)E_{\mathrm{t}}(\mathrm{Sn}) + \mu_{\mathrm{Sn}}\right] - x\left[E_{\mathrm{t}}(\mathrm{Ge}) + \mu_{\mathrm{Ge}}\right] \quad (2)$$

where $E_{\mathrm{t}}\left[\mathrm{Sr}_{1-x}\mathrm{Ge}_x\mathrm{SnO}_3\right]$ and $E_{\mathrm{t}}\left[\mathrm{SrSn}_{1-x}\mathrm{Ge}_x\mathrm{O}_3\right]$ are total energies of the alloys, $E_{\mathrm{t}}\left(\mathrm{SrSnO}_3\right)$ is the total energy of the host material, and E_{t} (Sr), E_{t} (Sn), and E_{t} (Ge), and are total energy per atom of the Sr, Sn, and Ge bulk phases, to which the chemical potentials μ_{Sr}, μ_{Sn}, and μ_{Ge} are referenced ($\mu_{\mathrm{Sr}}, \mu_{\mathrm{Sn}}, \mu_{\mathrm{Ge}} \leq 0$). These chemical potentials are not independent, but must satisfy the stability condition of the parent material SrSnO$_3$, i.e.,

$$\mu_{\mathrm{Sr}} + \mu_{\mathrm{Sn}} + 3\mu_{\mathrm{O}} = \Delta H^{\mathrm{f}}\left(\mathrm{SrSnO}_3\right) \quad (3)$$

avoiding the formation of secondary phases SrO, SnO$_2$, and GeO$_2$, i.e.,

$$\mu_{\mathrm{Sr}} + \mu_{\mathrm{O}} < \Delta H^{\mathrm{f}}(\mathrm{SrO}) \quad (4)$$

$$\mu_{\mathrm{Sn}} + 2\mu_{\mathrm{O}} < \Delta H^{\mathrm{f}}\left(\mathrm{SnO}_2\right) \quad (5)$$

and

$$\mu_{\mathrm{Ge}} + 2\mu_{\mathrm{O}} < \Delta H^{\mathrm{f}}\left(\mathrm{GeO}_2\right) \quad (6)$$

Combining Eqs. (3) and (4), we obtain $\mu_{\mathrm{Sn}} + 2\mu_{\mathrm{O}} > \Delta H^{\mathrm{f}}\left(\mathrm{SrSnO}_3\right) - \Delta H^{\mathrm{f}}(\mathrm{SrO})$, which together with Eqs. (5) and (6) limit the region in the μ_{Sn} vs. μ_{O} diagram where SrSnO$_3$ is stable, as shown in Fig. 6. The lines separating the region where the B-site alloys SrSn$_{1-x}$Ge$_x$O$_3$have lower formation enthalpies than the A-site alloys Sr$_{1-x}$Ge$_x$SnO$_3$, i.e., $\Delta H^{\mathrm{f}}[\mathrm{SrSn}_{1-x}\mathrm{Ge}_x\mathrm{O}_3] \leq \Delta H^{\mathrm{f}}[\mathrm{Sr}_{1-x}\mathrm{Ge}_x\mathrm{SnO}_3]$, are located in the upper right corner of the μ_{Sn} vs μ_{O} diagram.

We can see that SrSnO$_3$ and SrSn$_{1-x}$Ge$_x$O$_3$ alloys are only stable in the orange region at the center of Fig. 6, limited by the formation of SrO (left), GeO$_2$ (below), and SnO$_2$ (right). The conditions for which the formation enthalpies of the A-site alloys Sr$_{1-x}$Ge$_x$SnO$_3$ would be lower than that of B-site alloys SrSn$_{1-x}$Ge$_x$O$_3$ occur in a region of μ_{Sn} and μ_{O} chemical potentials where the secondary phase SnO$_2$ is most favorable to form, i.e., where SrSnO$_3$ itself is unstable. This result clearly indicates that Ge prefers the Sn octahedral site over the Sr site.

We also note that in the A-site alloys, the Ge atom displays a large offsite displacement toward 3 of the original 12 nearest-neighbor O atoms (along the [110] pseudocubic direction), with Ge–O distances of ~2.06 Å. This further indicates that Ge^{2+} on the Sr site is unstable. In contrast, Ge sits on the Sn octahedral sites in SrSn$_{1-x}$Ge$_x$O$_3$, with Ge–O distances of ~1.93 Å (equatorial) and of ~1.97 Å (apical), reflecting the tetragonal structure, and shows no offsite displacement. These results, again, reflect the fact that Ge strongly prefers the octahedral Sn site over the Sr site in SrSnO$_3$, consistent with our experimental observations.

Conclusion. In summary, we have demonstrated the growth of epitaxial Sn$_{1-x}$Ge$_x$O$_2$ and SrSn$_{1-x}$Ge$_x$O$_3$ films via hybrid MBE. AFM, HRXRD, XPS, and STEM characterization shows that the GTIP precursor can be used as an effective source of Ge for the growth of both rutile and perovskite oxides while allowing excellent surface morphology and structural quality. DFT calculations indicate that Ge strongly prefers the Sn site in SrSnO$_3$ as opposed to the Sr site. This work opens another synthetic route to achieving Ge-containing oxides. Future studies should build upon this work by exploring process parameters to achieve the pure germanate end-members, demonstration of a growth window, and applying hybrid MBE to other Ge-based oxides.

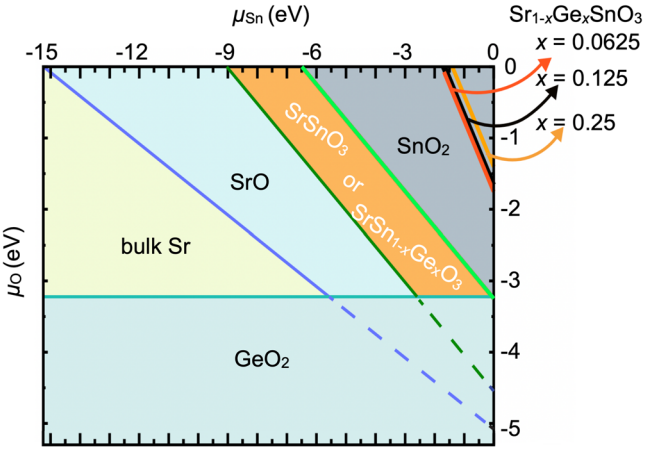

Fig. 6 Thermodynamic site preference of Ge in SrSnO$_3$. Calculated region in the tin chemical potential (μ_{Sn}) vs oxygen chemical potential (μ_{O}) plane showing where B-site alloys have lower formation enthalpy than the A-site alloys. The lines in the upper right corner ($x = 0.0625$, $x = 0.125$, and $x = 0.25$) separate the regions below which B-site alloys are preferred. This result indicates that for all allowed values of μ_{Sn} and μ_{O} for which SrSnO$_3$ is stable (orange region at the center), Ge will prefer to occupy the Sn site. The stability of SrSnO$_3$ is limited by the formation of SrO on the left (dark-green line, corresponding to) and the formation of SnO$_2$ on the right (light-green line), i.e., $\mu_{\mathrm{Sn}} + 2\mu_{\mathrm{O}} > \Delta H^{f}\left(\mathrm{SrSnO}_3\right) - \Delta H^{f}(\mathrm{SrO})$, and obtain $\mu_{\mathrm{Sn}} + 2\mu_{\mathrm{O}} < \Delta H^{f}\left(\mathrm{SnO}_2\right)$. The formation of GeO$_2$ poses a lower limit to the oxygen potential, as indicated in the bottom region, i.e., $\mu_{\mathrm{Ge}} + 2\mu_{\mathrm{O}} < \Delta H^{f}\left(\mathrm{GeO}_2\right)$. The formation enthalpy of A-site alloy will be lower than that of B-site alloy only in the upper right corner of the μ_{Sn} vs. μ_{O} diagram, a region where SrSnO$_3$ itself is unstable and SnO$_2$ is favorable to form.

Methods

Film growth. Sn$_{1-x}$Ge$_x$O$_2$ ($x = 0$, 0.28, 0.54) and SrSn$_{1-x}$Ge$_x$O$_3$ ($x = 0$, 0.05, 0.08, 0.16) films were successfully grown using hybrid MBE. This approach employs a conventional solid source for Sr where necessary, hexamethylditin (HMDT) as a metal–organic precursor for Sn, germanium tetraisopropoxide (GTIP) as a metal–organic precursor for Ge, and an inductively coupled RF plasma for O. Rutile films were grown on TiO$_2$(001) substrates at 600 °C, and perovskite films were grown on GdScO$_3$(110) substrates at 950 °C. When Sr was used, its beam equivalent pressure (BEP)—measured by a retractable beam flux monitor—was fixed at 2.3×10^{-8} Torr. For HMDT, the liquid precursor crucible and injector temperature were held at ~60 °C to achieve adequate vapor pressure, whereas the delivery lines were maintained at a slightly higher temperature of ~75 °C to prevent precursor condensation in delivery lines. Likewise, for GTIP, the liquid precursor was maintained at ~50 °C, the lines were maintained at ~65 °C, and the injector was maintained at ~70 °C. The BEPs of HMDT and GTIP were varied to control the Sn:Ge ratio in the films, although the final Ge fraction was not necessarily proportional to the BEP ratio. The oxygen flow was set to 0.7 sccm to achieve an oxygen background pressure of 5×10^{-6} Torr while applying 250 W RF power to the plasma coil. Each rutile film was grown for 60 min, and each perovskite film was grown for 30 min.

Film characterization. Surface topography was measured with a Bruker Nanoscope V Multimode 8 atomic force microscope (AFM). A Rigaku SmartLab XE was used for X-ray scattering. High-resolution X-ray diffraction (HRXRD) $2\theta-\omega$ coupled scans were used to determine out-of-plane lattice parameters. Film thickness was determined from HRXRD finite thickness fringes when possible, or otherwise

extracted from X-ray reflectivity (XRR). Reciprocal space maps (RSMs) were used to measure in-plane lattice parameters and determine strain relaxation. On each RSM, Vegard's law was used to calculate relaxed lattice parameters and Poisson ratios were used to calculate how the lattice parameters would change under biaxial stress. For the rutile system, lattice parameters were taken from powder neutron diffraction[20,21], and Poisson ratios were interpolated from elastic tensor data of the end-members[22,23]. For the perovskite system, substrate lattice parameters from Liferovich and coworkers[24] were used, whereas the $SrSnO_3$ tetragonal lattice parameters from Glerup and coworkers[25] and the parameters of ambient temperature (quenched) $SrGeO_3$ from Nakatsuka[26] were used for the film. Due to a lack of elastic tensor data for $SrGeO_3$, the DFT-predicted Poisson ratio for $SrSnO_3$ of 0.192[27] was used for the entire alloy series.

X-ray photoelectron spectroscopy (XPS) was used to determine the Ge fraction and valence. To determine composition, survey scans were measured using a Physical Electronics 5000 VersaProbe III photoelectron spectrometer with monochromatic Al K_α X-rays at the University of Minnesota. Empirical sensitivity factors from Wagner and coworkers were used[28]. To determine Ge valence, XPS was also performed at PNNL using an Omicron/Scienta R3000 analyzer with monochromatic Al K_α X-rays, a 100 eV analyzer pass energy, a 0.8 mm slit width, and a normal emission geometry. The resulting energy resolution was ~ 400 meV as judged by fitting the Fermi edge for a clean, polycrystalline Ag foil to the Fermi–Dirac function. The insulating nature of these films required the use of a low-energy electron flood gun to compensate the positive photoemission charge that builds up on the surface. The flood gun makes it possible to measure accurate core-level (CL) line shapes on insulating samples. However, the measured binding energies are artificially low due to overcompensation. At the same time, we sought to use a highly conductive *n*-Ge(001) crystal with its thin native oxide as an internal binding energy standard for Ge^0, Ge^{2+}, Ge^{3+} and Ge^{4+}, as assigned by Molle and coworkers[19]. In order to compare Ge 3*d* binding energies from the insulating MBE-grown films to those from the GeO_x/Ge standard, all samples were affixed to an insulating MgO(001) wafer in order to uniformly isolate them from the ground. The flood-gun beam energy was set to ~1 eV. The charging-induced binding energy shifts were close, but not identical, for the GeO_x/*n*-Ge sample and the epitaxial films, as judged by the aliphatic C 1 *s* peak binding energy from the surface contamination. After correcting for differences in charging as judged by the C 1 *s* binding energies, all spectra were shifted by a constant amount such that the Ge $3d_{5/2}$ lattice peak in the GeO_2/*n*-Ge spectrum fell at 29.4 eV, the value measured when GeO_2/*n*-Ge(001) is mounted directly on the grounded sample holder without an MgO wafer for electrical isolation.

Cross-sectional scanning transmission electron microscopy (STEM) samples were prepared using a FEI Helios NanoLab DualBeam Ga^+ Focused Ion Beam (FIB) microscope with a standard lift-out procedure. STEM high-angle annular dark-field (STEM-HAADF) images were collected on a probe-corrected JEOL GrandARM-300F microscope operating at 300 kV, with convergence semi-angle of 29.7 mrad and a collection angle range of 75–515 mrad. For the STEM-HAADF images shown in Fig. 5c, a series of ten frames was collected at 512 × 512 px sampling, with a dwell time of 2 μs px^{-1}. The images were rigid-aligned using the SmartAlign program to minimize drift and then averaged to improve signal-to-noise[29]. Simultaneous STEM energy dispersive X-ray spectroscopy (STEM-EDS) and electron energy-loss spectroscopy (STEM-EELS) elemental mapping were used to determine site occupation, using the Sn *L* peak and Sr *L* and Ge *L* edges, respectively. For this configuration, a STEM-EELS acceptance angle range of 113–273 mrad was used. Mapping was performed using a dual JEOL Centurio detector setup for STEM-EDS and a 1 eV ch^{-1} dispersion, with a 4× energy binning in the dispersive direction for STEM-EELS. No denoising was applied, but the composite map shown in Fig. 5d was filtered using a smoothing kernel in Gatan Microscopy Suite 3.4.3.

First-principles calculations. First-principles calculations were performed to investigate whether Ge prefers the octahedral Sn site with oxidation state 4+, or the Sr site with oxidation state 2+. The calculations are based on density functional theory[30,31] within the generalized gradient approximation revised for solids (PBEsol[32]), with projector augmented wave potentials[33,34] as implemented in the VASP code[35,36]. We considered both $SrSn_{1-x}Ge_xO_3$ and $Sr_{1-x}Ge_xSnO_3$ using supercells containing 80, 40, and 20 atoms representing concentrations $x = 0.0625$, 0.125, and 0.25, respectively. We used an energy cutoff of 500 eV for the plane wave expansions and meshes of k-points that are equivalent to 6 × 6 × 4 for the 20-atom cell of the tetragonal $SrSnO_3$. All the atom positions in the cell were allowed to relax. To simulate the epitaxial growth of the alloy on $GdScO_3$(110) substrates, we fixed the in-plane lattice parameters to that of $GdScO_3$, allowing the out-of-plane lattice parameter to relax together with all the atomic positions, minimizing the stress tensor and the total energy.

Data availability

The data that support the findings of this study have been included in the manuscript and supplementary information. Any additional data are available from the corresponding author upon reasonable request.

Received: 17 March 2022; Accepted: 9 September 2022;
Published online: 04 October 2022

References

1. Stapelbroek, M. & Evans, B. D. Exciton structure in the u.v.-absorption edge of tetragonal GeO_2. *Solid State Commun.* **25**, 959–962 (1978).
2. Chae, S., Lee, J., Mengle, K. A., Heron, J. T. & Kioupakis, E. Rutile GeO_2: an ultrawide-band-gap semiconductor with ambipolar doping. *Appl. Phys. Lett.* **114**, 102104 (2019).
3. Chae, S. et al. Toward the predictive discovery of ambipolarly dopable ultra-wide-band-gap semiconductors: the case of rutile GeO_2. *Appl. Phys. Lett.* **118**, 260501 (2021).
4. Chae, S. et al. Thermal conductivity of rutile germanium dioxide. *Appl. Phys. Lett.* **117**, 102106 (2020).
5. Chae, S., Paik, H., Vu, N. M., Kioupakis, E. & Heron, J. T. Epitaxial stabilization of rutile germanium oxide thin film by molecular beam epitaxy. *Appl. Phys. Lett.* **117**, 072105 (2020).
6. Takane, H. & Kaneko, K. Establishment of a growth route of crystallized rutile GeO_2 thin film (≧1 μm/h) and its structural properties. *Appl. Phys. Lett.* **119**, 062104 (2021).
7. Deng, G., Saito, K., Tanaka, T., Arita, M. & Guo, Q. Pulsed laser deposition growth of ultra-wide bandgap GeO_2 film and its optical properties. *Appl. Phys. Lett.* **119**, 182101 (2021).
8. Rowberg, A. J. E., Krishnaswamy, K. & Van de Walle, C. G. Prospects for high carrier mobility in the cubic germanates. *Semiconductor Sci. Technol.* **35**, 085030 (2020).
9. Mizoguchi, H., Kamiya, T., Matsuishi, S. & Hosono, H. A germanate transparent conductive oxide. *Nat. Commun.* **2**, 470 (2011).
10. Sasaki, S., Prewitt, C. T. & Liebermann, R. C. The crystal structure of $CaGeO_3$ perovskite and the crystal chemistry of the $GdFeO_3$-type perovskites. *Am. Mineralogist* **68**, 1189–1198 (1983).
11. Susaki, J., Akaogi, M., Akimoto, S. & Shimomura, O. Garnet-perovskite transformation in $CaGeO_3$: in-situ X-ray measurements using synchrotron radiation. *Geophys. Res. Lett.* **12**, 729–732 (1985).
12. Ross, N. L., Akaogi, M., Navrotsky, A., Susaki, J.-I. & McMillan, P. Phase transitions among the $CaGeO_3$ polymorphs (wollastonite, garnet, and perovskite structures): studies by high-pressure synthesis, high-temperature calorimetry, and vibrational spectroscopy and calculation. *J. Geophys. Res. Solid Earth* **91**, 4685–4696 (1986).
13. Ono, S., Kikegawa, T. & Higo, Y. In situ observation of a garnet/perovskite transition in $CaGeO_3$. *Phys. Chemistry Minerals* **38**, 735 (2011).
14. Jalan, B., Moetakef, P. & Stemmer, S. Molecular beam epitaxy of $SrTiO_3$ with a growth window. *Appl. Phys. Lett.* **95**, 032906 (2009).
15. Zhang, H.-T., Dedon, L. R., Martin, L. W. & Engel-Herbert, R. Self-regulated growth of $LaVO_3$ thin films by hybrid molecular beam epitaxy. *Appl. Phys. Lett.* **106**, 233102 (2015).
16. Prakash, A. et al. Adsorption-controlled growth and the influence of stoichiometry on electronic transport in hybrid molecular beam epitaxy-grown $BaSnO_3$ films. *J. Materials Chemistry C* **5**, 5730–5736 (2017).
17. Enslin, J. et al. Metamorphic $Al_{0.5}Ga_{0.5}N$:Si on AlN/sapphire for the growth of UVB LEDs. *J. Crystal Growth* **464**, 185–189 (2017).
18. Miceli, P. F. & Palmstrom, C. J. X-ray scattering from rotational disorder in epitaxial films: an unconventional mosaic crystal. *Phys. Rev. B* **51**, 5506–5509 (1995).
19. Molle, A., Bhuiyan, M. N. K., Tallarida, G. & Fanciulli, M. In situ chemical and structural investigations of the oxidation of Ge(001) substrates by atomic oxygen. *Appl. Phys. Lett.* **89**, 083504 (2006).
20. Burdett, J. K., Hughbanks, T., Miller, G. J., Richardson, J. W. & Smith, J. V. Structural-electronic relationships in inorganic solids: powder neutron diffraction studies of the rutile and anatase polymorphs of titanium dioxide at 15 and 295 K. *J. Am. Chem. Soc.* **109**, 3639–3646 (1987).
21. Bolzan, A. A., Fong, C., Kennedy, B. J. & Howard, C. J. Structural studies of rutile-type metal dioxides. *Acta Crystallographica Sec. B* **53**, 373–380 (1997).
22. Chang, E. & Graham, E. K. The elastic constants of cassiterite SnO_2 and their pressure and temperature dependence. *J. Geophys. Res.* **80**, 2595–2599 (1975).
23. Wang, H. & Simmons, G. Elasticity of some mantle crystal structures: 2. Rutile GeO_2. *J. Geophys. Res.* **78**, 1262–1273 (1973).
24. Liferovich, R. P. & Mitchell, R. H. A structural study of ternary lanthanide orthoscandate perovskites. *J. Solid State Chemistry* **177**, 2188–2197 (2004).
25. Glerup, M., Knight, K. S. & Poulsen, F. W. High temperature structural phase transitions in $SrSnO_3$ perovskite. *Mater. Res. Bull.* **40**, 507–520 (2005).
26. Nakatsuka, A., Arima, H., Ohtaka, O., Fujiwara, K. & Yoshiasa, A. Crystal structure of $SrGeO_3$ in the high-pressure perovskite-type phase. *Acta Crystallographica Sect. E* **71**, 502–504 (2015).

27. Shein, I. R., Kozhevnikov, V. L. & Ivanovskii, A. L. First-principles calculations of the elastic and electronic properties of the cubic perovskites $SrMO_3$ (M=Ti, V, Zr and Nb) in comparison with $SrSnO_3$. *Solid State Sci.* **10**, 217–225 (2008).
28. Wagner, C. D. et al. Empirical atomic sensitivity factors for quantitative analysis by electron spectroscopy for chemical analysis. *Surface Interface Anal.* **3**, 211–225 (1981).
29. Jones, L. et al. Smart Align—a new tool for robust non-rigid registration of scanning microscope data. *Adv. Struct. Chemical Imaging* **1**, 8 (2015).
30. Hohenberg, P. & Kohn, W. Inhomogeneous electron gas. *Phys. Rev.* **136**, B864–B871 (1964).
31. Kohn, W. & Sham, L. J. Self-consistent equations including exchange and correlation effects. *Phys. Rev.* **140**, A1133–A1138 (1965).
32. Perdew, J. P. et al. Restoring the density-gradient expansion for exchange in solids and surfaces. *Phys. Rev. Lett.* **100**, 136406 (2008).
33. Blöchl, P. E. Projector augmented-wave method. *Phys. Rev. B* **50**, 17953–17979 (1994).
34. Kresse, G. & Joubert, D. From ultrasoft pseudopotentials to the projector augmented-wave method. *Phys. Rev. B* **59**, 1758–1775 (1999).
35. Kresse, G. & Furthmüller, J. Efficiency of ab-initio total energy calculations for metals and semiconductors using a plane-wave basis set. *Comput. Mater. Sci.* **6**, 15–50 (1996).
36. Kresse, G. & Furthmüller, J. Efficient iterative schemes for ab initio total-energy calculations using a plane-wave basis set. *Phys. Rev. B* **54**, 11169–11186 (1996).
37. Mountstevens, E. H., Attfield, J. P. & Redfern, S. A. T. Cation-size control of structural phase transitions in tin perovskites. *J. Phys. Condensed Matter* **15**, 8315–8326 (2003).
38. Wang, T., Prakash, A., Warner, E., Gladfelter, W. L. & Jalan, B. Molecular beam epitaxy growth of SnO_2 using a tin chemical precursor. *J. Vacuum Sci. Technol. A* **33**, 020606 (2015).
39. Jalan, B., Engel-Herbert, R., Cagnon, J. & Stemmer, S. Growth modes in metal-organic molecular beam epitaxy of TiO_2 on r-plane sapphire. *J. Vacuum Sci. Technol. A* **27**, 230–233 (2009).
40. Jalan, B., Engel-Herbert, R., Wright, N. J. & Stemmer, S. Growth of high-quality $SrTiO_3$ films using a hybrid molecular beam epitaxy approach. *J. Vacuum Sci. Technol. A* **27**, 461–464 (2009).
41. Moyer, J. A., Eaton, C. & Engel-Herbert, R. Highly conductive $SrVO_3$ as a bottom electrode for functional perovskite oxides. *Adv. Mater.* **25**, 3578–3582 (2013).
42. Engel-Herbert, R., Hwang, Y., Cagnon, J. & Stemmer, S. Metal-oxide-semiconductor capacitors with ZrO_2 dielectrics grown on $In_{0.53}Ga_{0.47}As$ by chemical beam deposition. *Appl. Phys. Lett.* **95**, 062908 (2009).
43. Kajdos, A. P., Ouellette, D. G., Cain, T. A. & Stemmer, S. Two-dimensional electron gas in a modulation-doped $SrTiO_3/Sr(Ti,Zr)O_3$ heterostructure. *Appl. Phys. Lett.* **103**, 082120 (2013).
44. Alcock, C. B., Itkin, V. P. & Horrigan, M. K. Vapour pressure equations for the metallic elements: 298–2500 K. *Canadian Metallurgical Quarterly* **23**, 309–313 (1984).
45. Stull, D. R. In *American Institute of Physics Handbook* (ed. Dwight, E. G.) Ch. 4k (McGraw Hill, 1972).
46. Strephenson, R. M. & Malanowski, S. *Handbook of the Thermodynamics of Organic Compounds* (Elsevier, 1987).
47. Dykyj, J., Repas, M. & Svoboda, J. *Tlak Nasytenej Pary Organickych Zlucenin* (Vydavatelstvo Slovenskej Akademie Vied, 1984).
48. Cox, J. D. & Pilcher, G. *Thermochemistry of Organic and Organometallic Compounds* (Academic Press, 1970).

Acknowledgements

MBE growth of stannate (F.L., T.K.T., and B.J.) were supported by the U.S. Department of Energy through DE-SC002021. Germanate growth and characterization (F.L. and D.L.) were supported by the Air Force Office of Scientific Research (AFOSR) through Grants FA9550-21-1-0025 and FA9550-21-0460 and in part through NSF DMR-1741801. Parts of this work were carried out in the Characterization Facility, University of Minnesota, which receives partial support from the NSF through the MRSEC (Award Number DMR-2011401) and the NNCI (Award Number ECCS-2025124) programs. B.E.M., S.R.S., and S.A.C. carried out the STEM and XPS analysis with support from the U.S. Department of Energy, Office of Science, Division of Materials Sciences and Engineering under Award #10122 to Pacific Northwest National Laboratory (PNNL). PNNL is a multiprogram national laboratory operated for the U.S. Department of Energy (DOE) by Battelle Memorial Institute under Contract No. DE-AC05-76RL0-1830. STEM sample preparation was performed at the Environmental Molecular Sciences Laboratory (EMSL), a national scientific user facility sponsored by the DOE's Biological and Environmental Research program and located at PNNL. STEM imaging was performed in the Radiological Microscopy Suite (RMS), located in the Radiochemical Processing Laboratory (RPL) at PNNL.

Author contributions

F.L., T.K.T., and B.J. conceived the idea and designed experiments. Rutile films were grown and characterized with XRD and AFM by T.K.T. Perovskite films were grown and characterized with XRD and AFM by F.L. Composition determination with XPS was performed by D.L., F.L., and T.K.T. Oxidation state was determined via HAXPES by S.A.C. TEM was collected by B.E.M under the direction of S.R.S. I.L. performed DFT calculations under the direction of A.J. T.K.T., and F.L. wrote the manuscript with input from all authors. B.J. directed and organized the different aspects of the project.

Competing interests

The authors declare no competing interests.

Additional information

Supplementary information The online version contains supplementary material available at https://doi.org/10.1038/s43246-022-00290-y.

Correspondence and requests for materials should be addressed to Bharat Jalan.

Peer review information *Communications Materials* thanks the anonymous reviewers for their contribution to the peer review of this work. Primary Handling Editors: Zakaria Al Balushi and Aldo Isidori.